THE ASTROPHYSICAL JOURNAL, 490:682–697, 1997 December 1

DYNAMIC AND STOCHASTIC INFLUENCES ON SPIRAL STRUCTURE IN THE FLOCCULENT SPIRAL NGC 4414

MICHELE D. THORNLEY[1,2]
Max-Planck-Institut für extraterrestriche Physik, Postfach 1603, D-85740 Garching, Germany; and Department of Astronomy, University of Maryland, College Park, MD 20742

AND

LEE G. MUNDY[3]
Department of Astronomy, University of Maryland, College Park, MD 20742
Received 1997 May 8; accepted 1997 July 14

ABSTRACT

We present new Hα, CO, and H I images of the high gas surface density flocculent spiral NGC 4414 and compare them to recently published near-infrared observations that reveal kiloparsec-scale structures in the inner disk. The subtraction of an estimated supergiant contribution confirms that the near-infrared enhancements represent primarily variations in the surface density of the old stellar population. As material structures of kiloparsec extent cannot be maintained in a differentially rotating disk for sufficiently long times to be discernible in the old stellar population, the near-infrared observations suggest that global dynamical processes contribute to the formation of structure in NGC 4414. However, variations in the distribution of CO, H I, and Hα peaks with respect to near-infrared "arm" structures suggest that stochastic processes are also important.

Subject headings: galaxies: individual (NGC 4414) — galaxies: ISM — galaxies: kinematics and dynamics — galaxies: spiral — galaxies: stellar content — galaxies: structure — infrared: galaxies

1. INTRODUCTION

Grand-design spiral galaxies show enhanced emission along the spiral arms in a variety of tracers (see, e.g., Elmegreen & Elmegreen 1984; Kaufman et al. 1989; Rix & Rieke 1993; Deutsch & Allen 1993; Tilanus & Allen 1993; Knapen 1993; Gruendl 1996). Observations of these tracers, most notably, Hα, H I, CO, and near-infrared (NIR) emission, have provided theorists with an abundance of data for modeling the effects of moderate to strong density waves. NIR imaging in particular has revealed significant large-scale structure in the stellar distributions of a growing sample of galaxies, even in galaxies thought to be less affected by large-scale, dynamical processes (Regan & Vogel 1994, hereafter RV94; Thornley 1996; Grosbøl & Patsis 1996). As NIR emission is believed to trace the galactic potential via the emission from the old stellar population, such observations are able to probe global dynamical processes in a wide sample of spiral galaxies.

Structural information provided by NIR imaging is particularly valuable in studies of flocculent galaxies. By comparing NIR emission with tracers of the gas distribution (CO, H I) and recent star formation (Hα), the relative contributions of large-scale dynamical processes and local star formation to apparent structure in flocculent galaxies can be more carefully examined. Flocculent galaxies are defined by the "patchy, fleecelike" structures in their disks, which are suggestive of formation by local processes (Elmegreen & Elmegreen 1982, 1984, 1987). The work of Gerola, Seiden, & Schulman (Gerola & Seiden 1978; Seiden & Gerola 1979; Seiden & Schulman 1990 and references therein; collectively denoted as GSS) propose that all but the most strongly grand-design spirals have structure that can be created completely by stochastic, self-propagating star formation (SSPSF). However, armlike structures revealed in NIR imaging of nearby flocculents (Thornley 1996) consist of kiloparsec-scale, smooth components as well as small-scale, bright peaks that are distributed similarly to H II regions. The presence of such smooth components suggests that large-scale dynamics are important, even in flocculent galaxies. Indeed, in the flocculent spiral NGC 5055 the combination of NIR, CO, H I, and Hα data provides a strong case for the presence of low-amplitude spiral density waves (Thornley & Mundy 1997).

With deep NIR imaging to describe the properties of spiral arms over a wider range of arm strengths, it is now possible to examine more systematically the effects of large-scale dynamics on galactic disk properties such as the star formation rate. Though studies of global properties have questioned whether density waves have any effect on star formation (e.g., McCall & Schmidt 1986; Elmegreen & Elmegreen 1986; Stark, Elmegreen, & Chance 1987), studies of individual grand design spirals suggest that spiral density waves enhance star formation along the spiral arms (e.g., Vogel, Kulkarni, & Scoville 1988; Cepa & Beckman 1990; Lord & Young 1990). Recent studies have further suggested that increased star formation rates and efficiencies along spiral arms of grand-design galaxies such as M51 and M100 may be due to the formation of large molecular cloud structures in the regions of high gas density and low shear provided by the spiral arms (Rand 1993, 1995; Knapen et al. 1996). The presence of such large molecular gas structures, known as giant molecular associations (GMAs; Vogel et al. 1988; Rand & Kulkarni 1990; Rand 1993) or superclouds (Elmegreen 1994), in regions of enhanced star formation is

[1] Visiting Astronomer, Kitt Peak National Observatory, National Optical Astronomy Observatories, operated by the Association of Universities for Research in Astronomy, Inc., under contract with the National Science Foundation.

[2] mdt@hethp.mpe-garching.mpg.de.
[3] lgm@astro.umd.edu.

also consistent with the observed global correlation of star formation rates and gas surface densities (e.g., Kennicutt 1989). However, these conclusions were based only on observations of very strongly grand-design spiral galaxies.

Observations of the flocculent spirals NGC 4414 (Sakamoto 1996) and NGC 5055 (Thornley & Mundy 1997) indicate the presence of large cloud structures with similar properties to the GMAs found in grand-design spirals. The observation of GMAs in NGC 5055 may indicate that relatively weak density wave perturbations are sufficient to create large cloud structures. However, without a similar dynamical study, the significance of GMAs in NGC 4414 is unclear. A more detailed comparison of the distribution of gas and star formation tracers, with respect to the NIR morphology, is needed to determine the significance of large-scale processes, as well as whether such large-scale forces are necessary to produce the observed cloud structures. These questions are addressed herein, and an examination of star formation variations with respect to the NIR structures will be presented in a subsequent paper (Thornley 1997).

As much of this work is concerned with size scales of observed structure, it should be noted that we adopt a larger distance measurement than has been used previously. NGC 4414 has been placed by NIR Tully-Fisher and Type I supernovae measurements (Pierce 1994) at a distance of approximately 18 Mpc, rather than the value of 9.6 Mpc (Nearby Galaxies Catalog; Tully 1988) used in other recent studies (e.g., Braine, Combes, & van Driel 1993; Sakamoto 1996; Braine, Brouillet, & Baudry 1997). This change suggests that NGC 4414 is a normal-sized spiral with an optical diameter of $\sim$20 kpc. We will assume a distance of 18 Mpc to NGC 4414 throughout this paper. Though gas surface densities are unaffected, this change in distance does affect the determination of cloud masses and linear size scales.

In order to better understand the processes that create structure in NGC 4414, we present here a detailed comparison of published NIR broadband imaging with new Hα, CO, and H I observations on scales of 4″–30″ (350 pc to 2.6 kpc). Single-dish CO observations of NGC 4414 suggest that it has an average molecular gas surface density similar to that of M51, with CO emission detected over a significant fraction of the optical disk (Braine et al. 1993). Thus NGC 4414, with a similarly large molecular gas surface density but significantly less organized spiral structure, provides an interesting counterpart to M51. A summary of galaxy parameters for NGC 4414 is given in Table 1. The observations are described in § 2, an analysis of large-scale influences derived from Hα and NIR morphology is presented in § 3, and the response of the gas to the observed stellar structure is examined in § 4. The paper is summarized in § 5.

TABLE 1

NGC 4414: Galaxy Parameters

Type	SA(rs)c
d (Mpc)	18[a]
D_{25} (arcmin)	4.5[b]
Position angle (deg)	160[c]
Inclination (deg)	55[c]
Systemic velocity (V_{LSR}) (km s^{-1})	726 ($\pm$3)[c]
Center (K') (J2000):	
R.A. (h m s)	12 26 27.1[c]
Decl. (° ′ ″)	31 13 23.9[c]

[a] Pierce 1994.
[b] Nearby Galaxies Catalog (Tully 1988).
[c] This paper; see §§ 3.2, 4.2.

2. OBSERVATIONS AND DATA REDUCTION

2.1. Hα *Imaging*

The Hα emission from NGC 4414 was imaged in 1995 January, using the NOAO 0.9 m telescope at Kitt Peak. The T2KA CCD provides 0.″68 pixels over a 23.′2 field of view. The effective resolution of the observations was limited by the seeing to 2.″5. The narrowband Hα and continuum filters were 67 and 68 Å wide, centered on 6573 and 6653 Å, respectively; thus the contribution from [N II] was included in the Hα filter bandpass. Three integrations of 900 s each were acquired in both the Hα and continuum filters. Overscan subtraction, bias subtraction, and flat-fielding were accomplished using standard IRAF reduction tools. Final combination of the three integrations into a single image was accomplished using a χ^2 minimization routine by Regan & Gruendl (1995). Astrometry was performed using field stars from the Hubble Guide Star Catalog. Continuum subtraction was achieved by scaling the Hα and continuum filters to the same scale using the fluxes of unsaturated field stars and subtracting the scaled continuum image from the Hα image.

As the weather was not photometric, calibration was achieved by comparison with H II–region photometry using a calibrated Hα + [N II] image of NGC 4414 from a supernova study by van Dyk (1992). A linear regression fit to the fluxes of 10 H II regions gives a conversion factor $9.1 \pm 0.7 \times 10^{-18}$ ergs s^{-1} cm^{-2} counts^{-1}, with a correlation coefficient of 0.91 between flux and number of counts. To remove the contribution from [N II] emission, an estimate of the [N II]/Hα ratio was made using the average relation $\log([\mathrm{N\ II}]/\mathrm{H}\alpha) = -0.2(\mathrm{LC}) - 0.3$ (Kennicutt 1979), where LC is the van den Bergh luminosity class of the galaxy. A value of [N II]/Hα = 0.2 was used to correct for the inclusion of [N II] emission in the Hα bandpass, which is consistent with the range of values of [N II]/Hα in the sample of Kennicutt & Kent (1983). A correction for Galactic extinction was made, though this effect is extremely small: $A_B = 0.02$ (RC3; de Vaucouleurs et al. 1991), which corresponds to a brightness correction of 1% at the wavelength of Hα (Schild 1977). The factor to convert from observed counts in our Hα + [N II] image to brightness in Hα emission is 7.4×10^{-18} ergs s^{-1} cm^{-2} counts^{-1}. Given the narrower filters used in the van Dyk study, it is possible that [N II] emission was excluded from the bandpass for velocities covering the southeastern part of the galaxy. Because of added uncertainties in the inclusion of [N II] emission at all locations and the [N II]/Hα ratio in NGC 4414, we estimate the total uncertainty in the absolute calibration factor to be 25%. However, it should be kept in mind that the fluxes are also affected by variable internal extinction within NGC 4414, which may introduce uncertainties as large as 50%. We do not attempt to correct for this variable extinction.

2.2. *Molecular Gas*

To determine the molecular gas distribution on subkiloparsec scales, interferometer observations of the CO $J = 1$–0 line in two overlapping fields in NGC 4414 were acquired with the Berkeley-Illinois-Maryland Association

(BIMA) Array[4] (Welch et al. 1996). The two fields are aligned along the major axis and provide coverage of the inner 2.5 × 1.5 of NGC 4414. Observations were made in four configurations of six or nine antennas between 1995 February and 1996 April. The digital correlator was configured to provide 4 km s^{-1} resolution over the LSR velocity range 425–1000 km s^{-1}. Gain and phase calibration were accomplished through observations of 1310+323 every 15–30 minutes; passband corrections and absolute flux calibration were determined from observations of 3C 273. The synthesized beams for the two fields differ in size by less than 0.3.

The interferometer data were combined with the fully sampled single-dish CO observations of Braine et al. (1993), to obtain a complete image of the CO distribution. The combination was done using maximum entropy method (MEM) deconvolution software in the MIRIAD reduction and analysis package; the process is described in Thornley & Mundy (1997). The single-dish map was converted from main beam brightness temperature (in K) to flux (in Jy beam^{-1}) using a conversion factor of 4.8 Jy K^{-1}, based on a main beam efficiency of 0.60 (Braine et al. 1993). The input beam of the single-dish data was a Gaussian with 21″ FWHM. For the interferometer data, the average beam of 3.5 × 2.9 FWHM (P.A. −62.1) was used. To optimize the signal-to-noise ratio, the combined map was created with 8 km s^{-1} velocity channels and then convolved up to 3.75 resolution in the map plane. The rms noise in the combined map is 0.06 Jy beam^{-1} in an 8 km s^{-1} channel.

Comparison of maps made with interferometer data alone to the combined map described above indicates that the combined map detects 5%–10% more flux than the interferometer maps. The combined map, integrated over velocity, includes more than 87% of the single dish flux, summing all flux above the 2 σ level. Given the inherently positive nature of MEM deconvolution, it is difficult to obtain a reliable measure of the total flux at lower levels of emission. The interferometric data are sensitive to structure on size scales as large as 30″; if the remaining flux is distributed in structures larger than 30″, the average flux is approximately 0.02 Jy beam^{-1}, a factor of 3 lower than the noise level in the current map. Thus, we regard the combined map as an accurate representation of the CO flux distribution in the central region of NGC 4414.

2.3. *Atomic Gas*

H I observations were made with the NRAO Very Large Array (VLA)[5] in C and D arrays between fall 1994 and spring 1995. The quasar 3C 286 was observed as a flux and bandpass calibrator, and 1225+368 was used as a phase calibrator. Observations were taken in 2AC correlator mode, with on-line Hanning smoothing. This mode provided 64 channels with 10 km s^{-1} resolution, centered on $V_{\rm LSR}$ = 711 km s^{-1}. Bandpass and gain calibration were accomplished using standard AIPS reduction techniques.

In order to provide resolution which could distinguish structures on approximately kiloparsec scales, H I maps were made with robust weighting. Developed by Briggs (1995a, 1995b), robust weighting is a hybrid weighting scheme that includes information about the thermal noise characteristics of the data as well as the sampling in the (u, v) plane; it thus can provide images at higher resolution than natural weighting with minimal increase in the rms noise level. In this scheme, the weighting in regions of sparse (u, v) sampling is effectively natural, while the weighting in densely sampled regions is effectively uniform. To describe structures on larger scales and extending to larger radii, we also present a naturally weighted map. Both maps were created and cleaned using the AIPS routine IMAGR. The robustly weighted map was made with a robustness factor of zero, with a resulting synthesized beam of 17.5 × 15.3 (P.A. 72.1) and a noise level of 0.45 mJy beam^{-1} in a 10 km s^{-1} channel. The naturally weighted map has a synthesized beam of 34.4 × 32.6 (P.A. 61.1) and a noise level of 0.41 mJy beam^{-1} in a 10 km s^{-1} channel. All subsequent analysis, including creation of moment maps and modeling of the velocity field, was completed within the GIPSY analysis package.

2.4. *Creation of Integrated Emission and Velocity Maps*

Maps of integrated emission and emission-weighted peak velocity were created for both the CO and H I data. For consistency throughout this paper, we have assumed P.A. = 160°, i = 55° for NGC 4414 in the determination of large-scale parameters; these are the average values of position angle and inclination over the optical disk, as determined kinematically from the H I data (see § 4.2). The moment maps were created using a windowing technique, which includes all emission stronger than a specified cutoff appearing in two or more contiguous velocity channels. The zero-moment maps were made using a 2 σ cutoff, and the first moment maps were made with a 3 σ cutoff. Because of the positive bias of the MEM technique used in the reduction of the CO data, the H I velocity field was used as a mask in calculating the zero-moment CO maps. All emission was included that was greater than 2 σ in at least two adjacent velocity channels within 150 km s^{-1} of the expected velocity in each pixel. This masking is coarse enough to prevent artificial agreement of CO and H I velocities. Emission was detected over the velocity range 510–940 km s^{-1}.

The integrated CO intensities were converted to face-on molecular hydrogen surface densities using the relation N_{H_2} [cm^{-2}] = $XI_{\rm CO}$ cos i, where X is the CO-to-H_2 conversion factor and i is the inclination of the galaxy. A value of $X = 3 \times 10^{20}$ cm^{-2} [K km s^{-1}]$^{-1}$ was used for the CO-to-H_2 conversion factor (Strong et al. 1988; Scoville & Sanders 1987). Little is known about the metallicity of NGC 4414, so it is difficult to determine how severely it affects the value of X (see, e.g., Wilson 1995). Braine et al. (1997) suggest that X varies by a factor of 3 over the disk because of a changing excitation temperature with radius, but the uncertainties are large enough to be consistent with the value of X assumed here. The conversion factor from integrated flux to molecular hydrogen surface density, corrected for inclination, is Σ_{H_2} [$M_\odot$ pc^{-2}] = 18.1 $S_{\rm CO}$ [Jy beam^{-1} km s^{-1}].

The standard conversion from H I integrated intensity to H I column density, assuming optically thin emission, was used. The H I surface density radial profiles were made assuming a constant inclination, though variations in position angle and inclination are suggested by tilted-ring models to the velocity field (see § 4.2). The conversion factor

[4] The BIMA Array is operated by the Berkeley-Illinois-Maryland Association under funding from the National Science Foundation.

[5] The National Radio Astronomy Observatory is a facility of the National Science Foundation operated under cooperative agreement by Associated Universities, Inc.

from integrated flux to atomic hydrogen surface density, including a (cos i) correction for inclination, is $\Sigma_{\rm H\,I}$ [$M_\odot$ pc^{-2}] = 19.2 $S_{\rm H\,I}$ [Jy beam^{-1} km s^{-1}] for the robustly weighted map and $\Sigma_{\rm H\,I}$ [$M_\odot$ pc^{-2}] = 4.55 $S_{\rm H\,I}$ [Jy beam^{-1} km s^{-1}] for the naturally weighted map.

3. DISTRIBUTION OF YOUNG AND OLD STARS: OBSERVATIONS AND IMPLICATIONS

In this section we examine the distribution of the old stellar population and recent star formation. After a brief discussion of the global star formation rate inferred from the Hα image, a comparison of Hα and NIR emission is pursued, to show the significance of the NIR arm structures reported by Thornley (1996). This comparison suggests that stochastic star formation is not the only important factor in the creation of structure in flocculent spirals.

3.1. *Tracing Star Formation with* Hα *Emission*

The Hα image, shown in Figure 1, displays a relatively stochastic distribution of star forming regions. As noted in a survey of nuclear Hα emission by Pogge (1989), there is a significant depression in Hα emission in the central region of NGC 4414. This may be due to a change in the stellar colors in the bulge, which would mask weak Hα emission in the continuum subtraction. With the improved resolution and sensitivity, as well as a larger field of view, the H II regions are better resolved in our data. Several pairs or short chains of H II regions appear over the inner part of the galaxy, and bright H II regions lie at greater radii on the north side of the galaxy than on the south.

To convert the observed Hα emission into a total star formation rate (SFR), we use the models of Kennicutt (Kennicutt 1983; Kennicutt, Tamblyn, & Congdon 1994). The SFR was determined from the revised conversion relation of Kennicutt et al. (1994):

$$\mathrm{SFR}(M > 0.1\ M_\odot) = \frac{L_{\rm H\alpha}}{1.36 \times 10^{41}\ \mathrm{ergs\ s^{-1}}}\,,$$

where SFR is in units of $M_\odot$ yr^{-1}. The total integrated flux of the Hα image is 1.79×10^{41} ergs s^{-1}, which implies a total SFR of 1.3 $M_\odot$ yr^{-1}. This is comparable to the average value for the 59 Sc galaxies listed in Kennicutt (1983), when the average extinction correction ($A_{\rm H\alpha}$) and the new calibration relation of Kennicutt et al. (1994) are taken into account. The global star formation rate in M51, on the same scale, is 2.0 $M_\odot$ yr^{-1}, comparable to the average for the 13 Sbc galaxies in the Kennicutt sample. The largest uncertainty in the comparison of the SFRs from individual galaxies is the amount of internal extinction. While the average extinction in M51 is $A_V = 2$ (van der Hulst et al. 1980), the extinction in NGC 4414 is unknown; however, the similarities in the molecular gas density may suggest that the average extinction in NGC 4414 is similar to that in M51 (see § 3.3). If this is the case, then the SFR may be

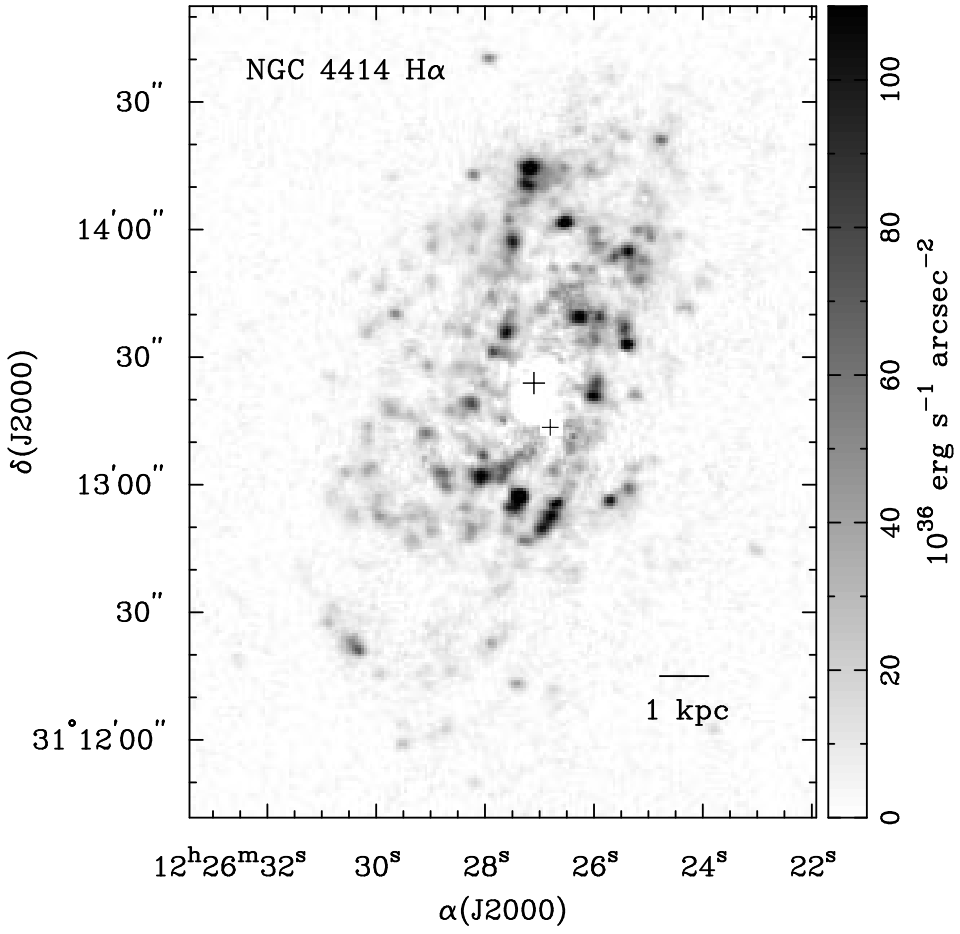

FIG. 1.—Hα image of NGC 4414. The K'-band center and the foreground star are marked by black crosses. The region around the foreground star has been masked out in this image. The scale bar at right shows Hα brightness in units of 10^{36} ergs s^{-1} arcsec^{-2}.

somewhat depressed with respect to that in M51, but not significantly so. The difference between the SFRs in the two galaxies is comparable to the difference between the average SFR values for their respective Hubble types and thus does not necessarily indicate any differences in the SFR due to the organization of the spiral arms in each galaxy. A more detailed analysis of the properties of star formation in NGC 4414 and their relation to the molecular gas morphology and NIR structure will be presented in a subsequent paper (Thornley 1997).

3.2. *Comparison of* Hα *and NIR Morphologies*

The K' residual image of Thornley (1996) shows short, irregular "arm" segments extending to radii of 40″–55″ (∼4–5 kpc) (Fig. 2, *left panel*). There is a suggestion of rough, four-arm structure and a ring or tightly wound arms near the center at a radius of 20″ (∼2 kpc). Two components to the emission are evident: a small-scale, peaked component and a smooth, extended component. To isolate the small-scale structures, an unsharp masked image was made by subtracting a smoothed image of the K' data, created by smoothing with a Gaussian of 5″ FWHM, from the original K' image. The unsharp masked image is also shown in Figure 2 (*right panel*). As smooth features in the residual map have characteristic widths of ∼10″, the unsharp masked image highlights structures on smaller scales. Although there is significant oversubtraction in the central region, due to the bright bulge and a foreground star to the southwest of the nucleus, a pattern of peaks similar to the distribution of bright H II regions can be seen. These peaks are 4–5 times fainter in the unsharp masked image than in the residual image. A significant fraction of the peaks are detected along the "arm" structures.

It has been suggested by several authors (e.g., Rix & Rieke 1993; RV94; Gruendl 1996) that this small-scale, peaked distribution arises from the NIR contribution of young red supergiants. Figures 1 and 2 demonstrate a good correlation between star-forming regions, as traced by Hα, and the peaks in K' emission. This correspondence supports the argument that a significant fraction of the small-scale NIR emission traces relatively young K and M supergiants rather than the old stellar population. In the next section, we examine the significance of these small-scale contributions to the appearance of larger scale NIR "arm" structures.

3.3. *Supergiant "Contamination" and Near-Infrared Structure*

Both Rix & Rieke (1993) and RV94 suggest that supergiants make significant contributions to NIR emission only on small scales, in the vicinity of H II regions, where their massive progenitors formed. However, even if the contribution from supergiants is a small fraction of the integrated K-band emission, this contribution may be a significant portion of the observed arm enhancements when the arm emission is only 20%–40% higher than in the interarm regions (Thornley 1996). Given the low-level enhancement and lack of overall symmetry of arm structures in NGC 4414, it is important to ascertain whether the observed structures can be accounted for solely by recent star formation.

RV94 suggest the use of Hα emission as a tracer of red supergiants and used the models of Bruzual & Charlot (1993) to determine the scaling between Hα luminosity and the K-band contribution from red supergiants. Gruendl (1996) applied this model to create a map of the supergiant "contamination" in M51; comparison of this "contamination map" with an unsharp-masked K' image shows the morphologies to be similar. Encouraged by these results, we explored the technique of removing a

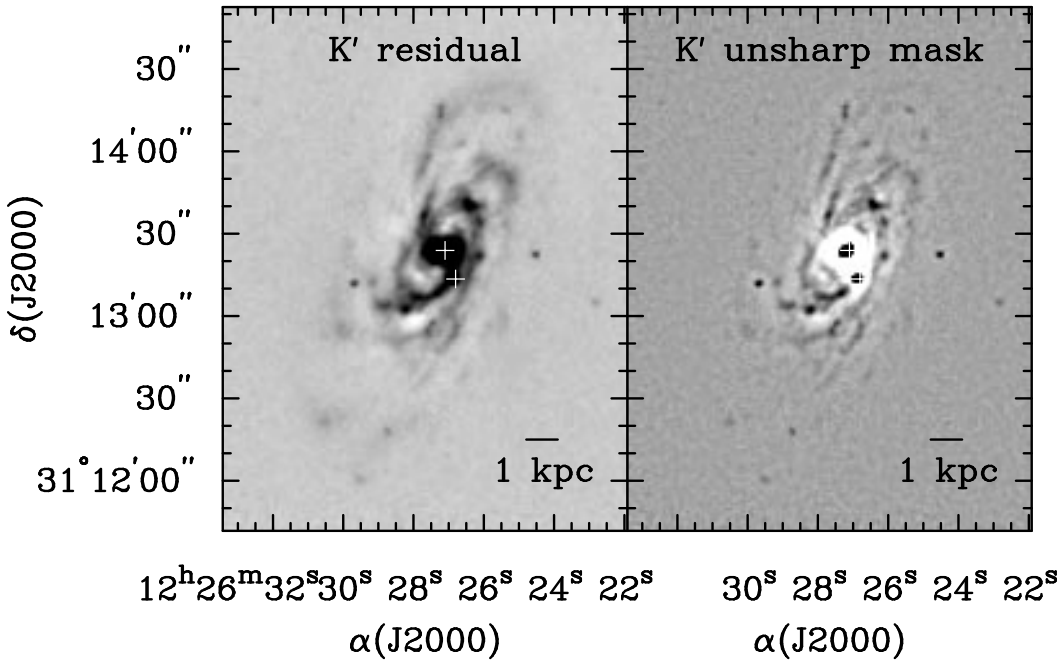

FIG. 2.—*Left panel: K′* residual image of NGC 4414, from which axisymmetric bulge and disk models have been subtracted (Thornley 1996). Central K' emission peak and foreground star are marked with white crosses. A linear scale bar is shown at lower right. The effective resolution is 2″. *Right panel:* Unsharp-masked image of K' emission in NGC 4414. Oversubtraction caused by the bright nucleus and the foreground star southwest of the center is evident. The intensity scale of this figure is a factor of 2 smaller than in the residual image, in order to highlight small-scale features.

"contamination" component from the disk- and bulge-subtracted residual K' image, in order to better understand the nature of the spiral structure in NGC 4414.

Although the K-band supergiant luminosity estimated by Hα emission has an inherent uncertainty because the red supergiants peak later than the OB stars that contribute to the Hα emission, RV94 estimated that from 10^7 to 10^8 yr after the onset of star formation for an instantaneous burst,

$$M_K > -2.5 \log \left(\frac{L_{\mathrm{H}\alpha}}{8.4 \times 10^{33} \text{ ergs s}^{-1}} \right),$$

where M_K is the K-band magnitude of the supergiant contribution in a star-forming region. Using this relation, the measured (from the unsharp masked image) and inferred (from the scaled Hα image) K-band magnitudes of the 12 brightest H II regions in NGC 4414 were compared. The supergiant contribution determined from the Hα observations accounts for 10%–40% of the K'-band emission in the unsharp masked image, with an average of 23%. The uncertainties in this comparison are large: as the subtraction of a smoothed image inherently underestimates the brightness of peaked structures and oversubtracts regions near the bulge, the fluxes of features in the unsharp masked image are likely only accurate to within a factor of 2. In addition, the amount of internal extinction in NGC 4414 and its variability are unknown. Last, the conversion factor between Hα and K-band emission offered by RV94 is relatively uncertain; it is dependent on assumptions about the initial mass function and star formation history of a region.

For a more conservative estimate, we opted to directly scale the Hα image by the residual K' image, using the fluxes of four Hα peaks and their corresponding K' residual peaks, which are well separated from the larger scale, smooth NIR enhancements. On average, K-band fluxes predicted from the Hα using the RV94 conversion factor are 8 times lower than the fluxes determined from scaling the Hα image by the K' residual map. This apparent discrepancy may be accounted for partially by extinction due to the high molecular gas surface densities in NGC 4414 (see § 4.1). The average extinction toward H II regions in M51, a galaxy with similar gas surface densities, is $A_V \sim 2$ (van der Hulst et al. 1980). This corresponds to $A_{\mathrm{H}\alpha} = 1.7$, or a factor of 5 in brightness.

By subtracting the scaled Hα image from the K' residual image, we produce a "decontaminated" K' image (Fig. 3). The "decontaminated" image, hereafter called the NIR image, shows reduced small-scale emission (in fact, oversubtraction of some H II regions is evident), but the kiloparsec-scale structures remain. The comparison of Figures 2 and 3 indicates that most of the emission in Figure 2 represents enhancements in the surface density of the old stellar population and thus traces the gravitational potential.

3.4. *Dynamical versus Stochastic Enhancements*

What is the source of these fluctuations in the stellar potential? While the lack of azimuthal symmetry suggests that the structures are not caused by a simple dynamical perturbation such as a pure $m = 2$ spiral density wave or a bar, it is difficult to maintain kiloparsec-scale structures in regions of differential rotation without the assistance of a large-scale, organizing influence. The structures in NGC 4414 cover radii from 20″–55″ (2–5 kpc); as the rotation curve is rising only slowly, even at the innermost points (see § 4.2), these structures cannot be material "arms" maintained by solid-body rotation.

The numerical simulations of GSS have shown that it is possible to create large-scale arm structures with only localized processes. In the SSPSF model, one star-forming complex will cause the formation of other star-forming complexes, which spread out like "beads on a string" due to differential rotation. In optical bands, the young stars would fade in brightness and be replaced by new stars, thus

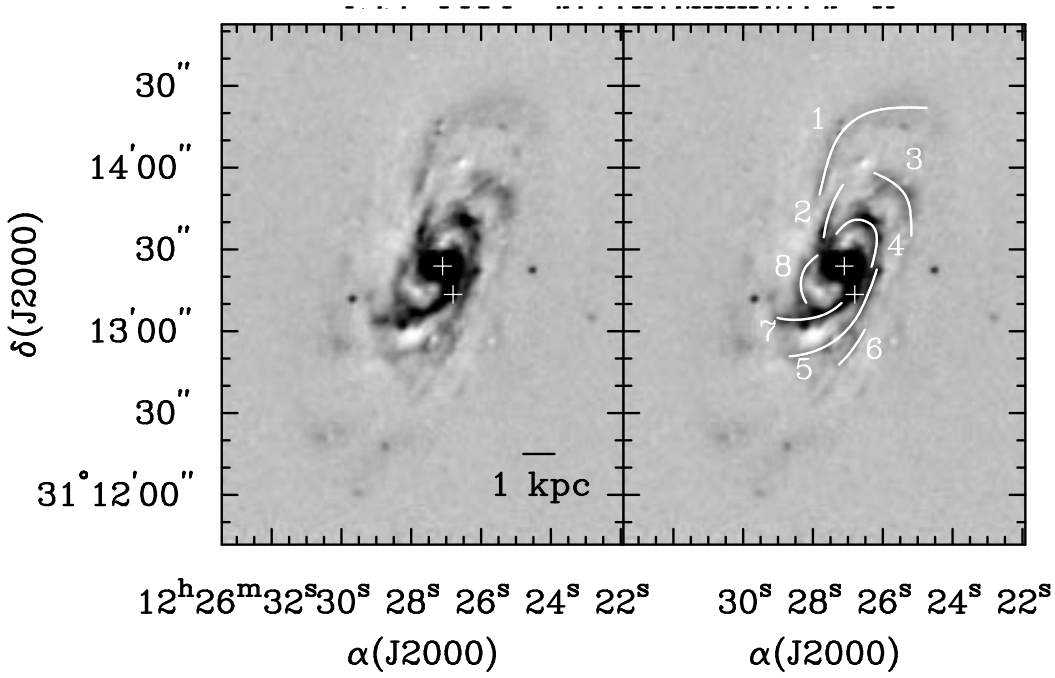

FIG. 3.—*Left panel:* "Decontaminated" K' image of NGC 4414, from which bulge and disk models, as well as an estimate of the contribution from red supergiants, have been subtracted. *Right panel:* The same image, overlaid with the eight residual structures defined in § 3.3. A spline fit was used to define these structures.

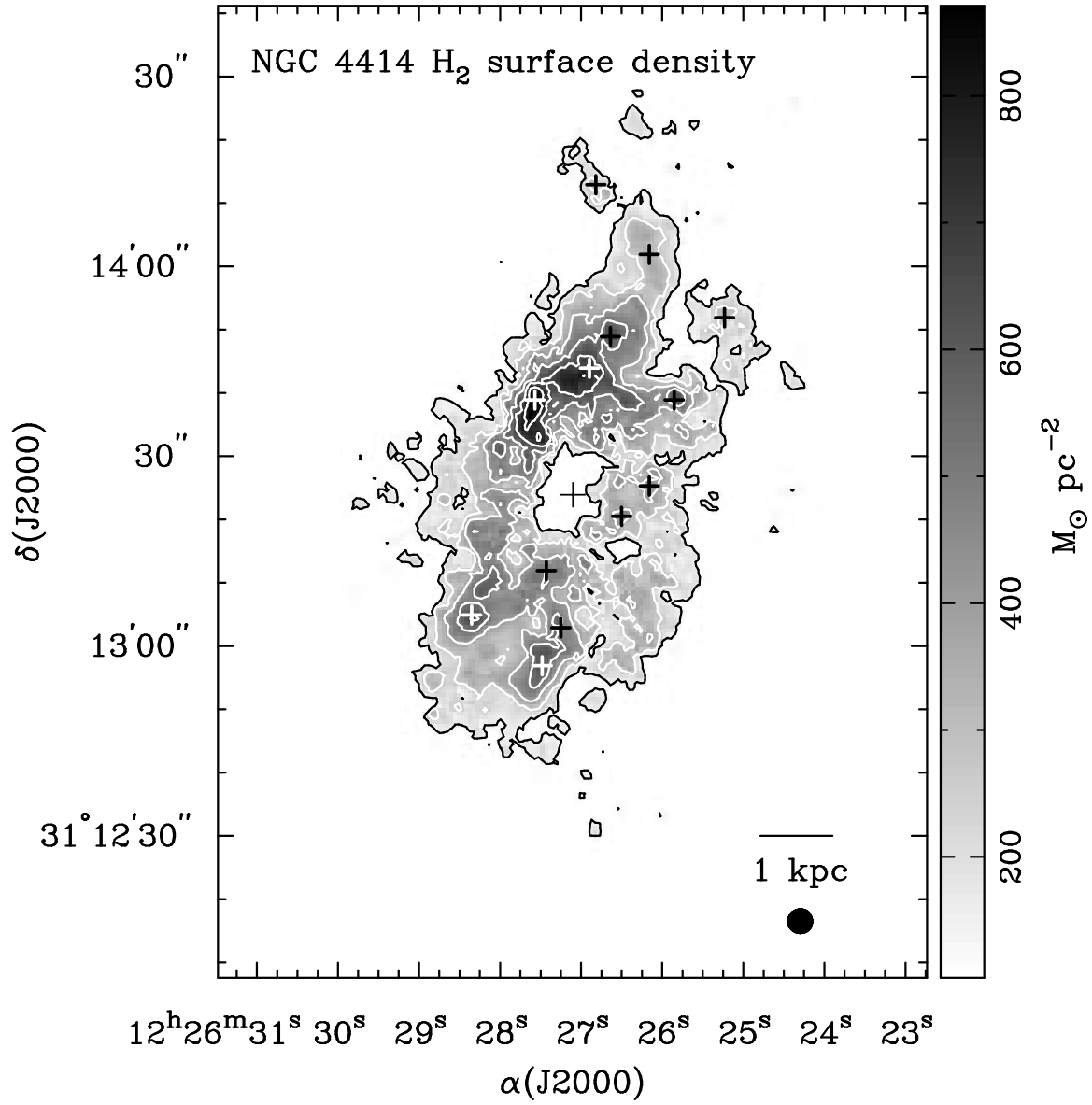

FIG. 4.—H_2 surface density map of NGC 4414 in units of $M_\odot$ pc^{-2}, uncorrected for inclination. The outer black contour indicates a surface density of 140 $M_\odot$ pc^{-2}, and the white contours indicate surface densities of 260, 390, 520, 650, and 780 $M_\odot$ pc^{-2}. The K'-band center is marked with a cross, and the positions of the 13 GMAs are noted with thick plus signs (*black and white*). The beam and linear scale bar are shown at lower right.

maintaining the apparent spiral structure. However, such models are strongly constrained by NIR observations: in the near-infrared, the fading emission from supergiants is replaced by the increasing contribution from lower mass stars as they evolve.

Simple arguments can be used to show the difficulties of maintaining NIR spiral structure that is produced by purely stochastic means. For example, at a radius of 3–5 kpc in NGC 4414, one galactic rotation is completed in approximately 10^8 yr. If we take an average star-forming complex in NGC 4414, with a diameter of approximately 400 pc (Elmegreen et al. 1994), and place it at a radius of 4 kpc, it will be stretched to a length of 2–3 kpc in one orbit by differential rotation. According to the models of Bruzual & Charlot (1993, see their Fig. 2), AGB stars contribute a significant fraction of the K-band light after a few times 10^8 yr and the majority of the K-band luminosity from $\sim 5 \times 10^8$–10^9 yr. In the same models, low-mass giant stars become the dominant source of K-band light after a few times 10^9 yr. Thus, in the time it takes for the more evolved intermediate- and low-mass stars (which likely produce the smooth enhancements seen in Fig. 3) to dominate K-band emission, the single star-forming complex will have made several revolutions around the galactic center, be stretched to a length of 10 kpc or more, and cover an azimuthal angle of more than 140°. Combining this structure with those formed from other star-forming complexes distributed around the galaxy at similar radii, any apparent structure formed by this process would quickly wind up and disappear.

This limitation was noted by Seiden & Gerola (1979), who used the multiband models of Struck-Marcell & Tinsley (1978) to show that any K-band spiral structure formed by the SSPSF model is completely smoothed out over time (see Seiden & Gerola 1979, their Fig. 6). These earlier models did not include contributions from AGB

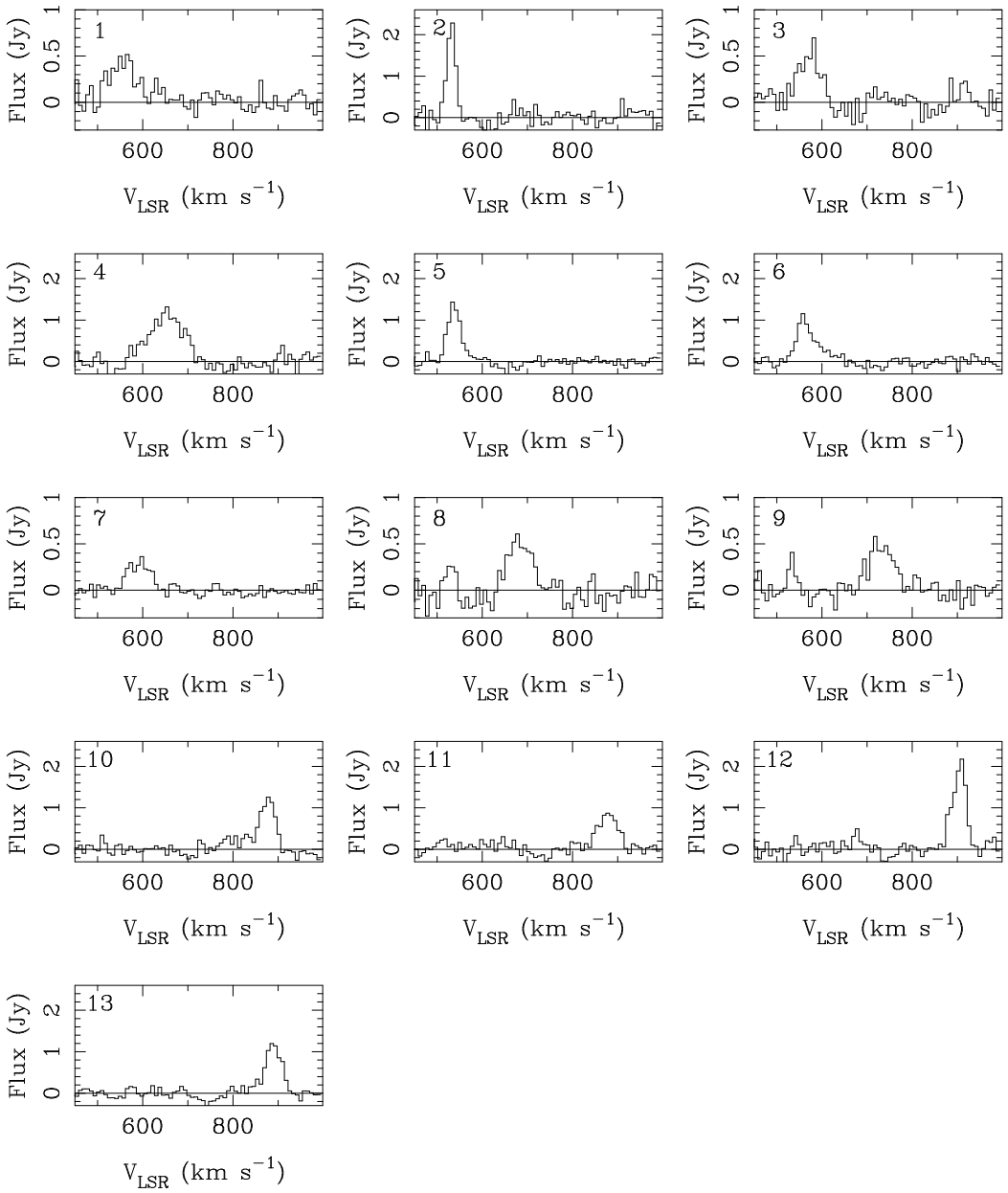

FIG. 5.—Spectra of the 13 GMAs measured in § 4.1, created by summing the emission over each structure. Number in upper left-hand corner of each panel corresponds to the GMA number given in Table 2.

stars; however, the contribution from these intermediate-mass stars only makes the problem of maintaining distinct spiral structures more severe. Thus the "armlike" structures seen in the inner disk of NGC 4414, despite their lack of symmetry, must be formed by long-term, dynamical processes.

To further study the properties of NGC 4414 in the vicinity of the NIR structures, we have identified eight structures in the NIR image that have projected lengths of more than 1 kiloparsec. Spline fits to these structures are overlaid and numbered on the NIR image in Figure 3. The identification of these structures does not necessarily imply that they are separate physical structures; they are defined here only to facilitate direct comparison with structures at other wavelengths.

4. RESPONSE OF MOLECULAR AND ATOMIC GAS

We have shown that the NIR structures in NGC 4414 likely have a dynamical origin; these dynamics should also affect the gas distribution. The response of both gas and stars to a variation in the gravitational potential should produce an alignment of observed NIR arms and gas structures, as well as perturbations in the velocity field. In this section, we search for signatures of such large-scale dynamics in the morphology and kinematics of CO and H I in NGC 4414.

4.1. *Molecular and Atomic Gas Distribution*

The map of H_2 surface density, derived from the combined map of CO integrated intensity, is shown in Figure 4. This map confirms the depression of CO emission in the center of the galaxy previously noted by Braine et al. (1993) and Sakamoto (1996). Although the FWHM of the combined primary beam pattern for our image is $160'' \times 100''$, very little emission is detected beyond the region mapped by Sakamoto (1996, with $65''$ FWHM primary beam). The

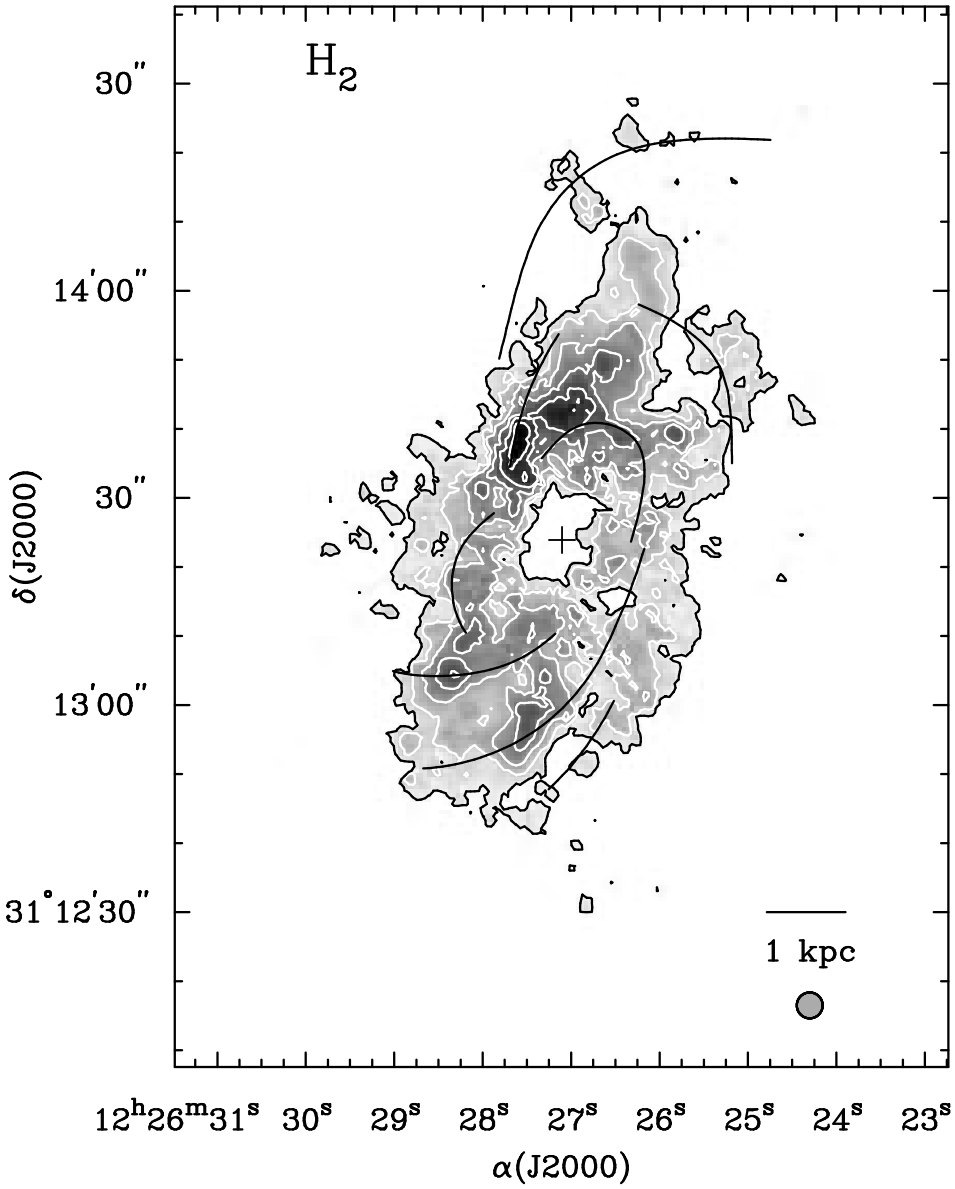

FIG. 6.—H_2 surface density map from the CO data, overlaid with the NIR arm segments from Fig. 3. The contours are the same as in Fig. 4. The beam is shown at lower right.

only exceptions are found to the northern side of the galaxy, where additional emission extends 35″–50″ from the center. This emission appears to be associated with bright H II regions on the north side of the galaxy. The maps presented in Figure 4 and in Sakamoto (1996) have similar overall morphologies, with some variations in the peaks to the north and south extremes of the emission distribution. The molecular gas surface density in NGC 4414 is very high: the peak H_2 surface densities (corrected for inclination) are 300–500 $M_\odot$ pc^{-2}, and surface densities exceed 80 $M_\odot$ pc^{-2} out to 0.75 R_{25}.

It is difficult to distinguish individual cloud structures over the mapped area; this may be due to the presence of a large-scale smooth gas component, or it may result from difficulties in resolving individual structures at this distance, especially in the inner parts of the galaxy. A median profile of the surface density distribution, which minimizes the contributions from bright peaks, shows an average value of 175 $M_\odot$ pc^{-2} for $10'' < r < 30''$ and drops to ~ 80 $M_\odot$ pc^{-2} at the largest detected radii. In position-velocity diagrams, the individual peaks are well separated at flux levels corresponding to the median surface density, suggesting that the emission can be viewed as arising from clumps on top of a smooth background component. Therefore, the properties of clumps were determined by measuring the fluxes and sizes of well-separated peaks after the subtraction of the median surface density. Note that this method yields a lower limit to the fluxes, and thus the masses, of individual features. On average, the flux determined from these clumps is a factor of 2 lower than if all flux over the same spatial region were included in the integrated flux.

We have identified 13 clumps that satisfy the following criteria: (1) the clump is resolved in at least one direction, (2) the peak of the clump is separated from neighboring clumps by more than a beamwidth, and (3) the clump is distinct from neighboring clumps at the half-power point of the clump after the median subtraction. The spectra of the clumps, obtained by summing the emission over the spatial

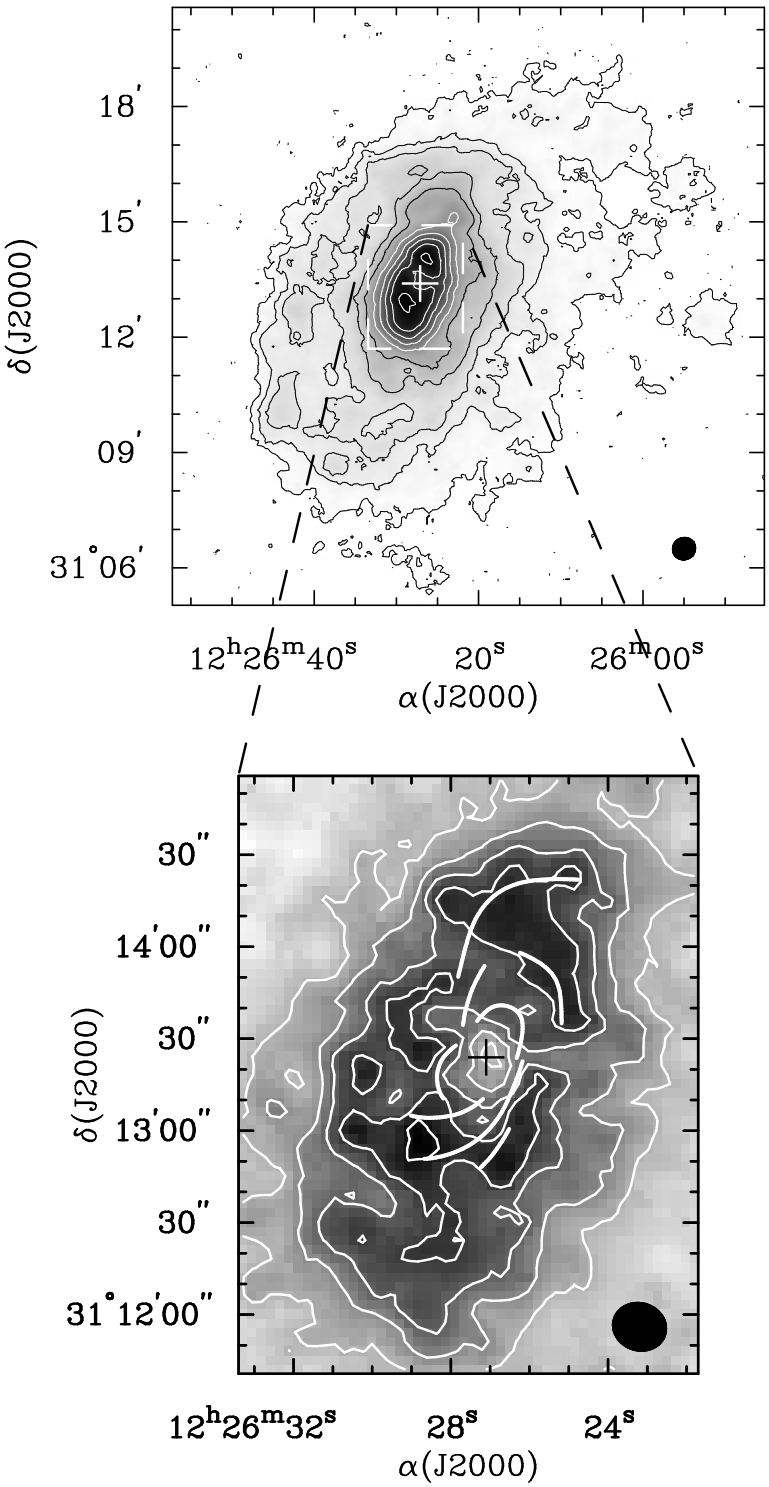

FIG. 7.—H I surface density map, uncorrected for inclination. The K' peak is marked in both panels. The top panel shows the naturally weighted map, with contours at 0.17, 0.35, 2.1, 3.8, 5.6, 8.2, 10.8, …, 18.6×10^{20} H atoms cm^{-2}. The bottom panel shows the inner region of the robustly weighted map covering the same area as in Fig. 2. The contours mark every 4.4×10^{20} H atoms cm^{-2}, from 8.7 to 26.3×10^{20} H atoms cm^{-2}. The beam is shown in the lower right corner of each image, and the NIR arm segments from Fig. 3 are overlaid on the bottom panel.

area of each structure, are shown in Figure 5. The locations, masses, and sizes of the clumps are tabulated in Table 2. As the properties of these structures are similar to those of GMAs previously reported (Vogel et al. 1988; Rand & Kulkarni 1990; Rand 1995; Sakamoto 1996; Thornley & Mundy 1997), they will be called GMAs throughout the rest of this paper. This sample partially overlaps with the eight "disk-GMAs" described in Sakamoto (1996) and includes three GMAs to the north which could only be measured in our larger map. The average GMA size in our map is $\sim 6''$, which corresponds to a diameter of 550 pc. The flux-based masses were determined using the formula $M_{\rm mol}[M_\odot] = 1.60 \times 10^4\, d^2_{\rm Mpc}\, S_{\rm CO}[\rm Jy\ km\ s^{-1}]$, where $S_{\rm CO}$ is the integrated flux and d is the distance to the galaxy. The flux-based

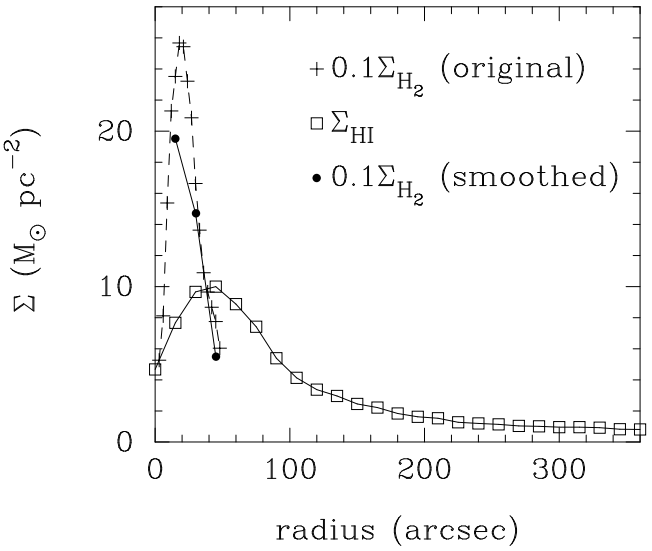

FIG. 8.—Azimuthally averaged radial profiles of H_2 (as determined from the CO data) and H I surface density. The crosses show the H_2 surface density profile at the original resolution of the CO data, multiplied by a factor of 0.1. The open squares mark the H I surface density determined from the robustly weighted map. The filled circles denote H_2 surface density, derived from the CO map after convolving to the same spatial resolution as the robustly weighted H I map and multiplied by 0.1. All profiles were derived assuming an inclination of 55°. The horizontal axis is radius in arcseconds, where 1″ = 87 pc at a distance of 18 Mpc.

masses of the GMAs measured here range from 1×10^7–3×10^8 $M_\odot$. With the exception of the three GMAs on the northern end of the major axis, all were detected in the inner part of the disk where velocities are changing quickly, and the projection of the galactic velocity field makes a large contribution to observed line widths. In particular, GMA 4 is an extended structure and may have contributions from multiple components that are not separable with the current resolution. Given the large uncertainties in determining intrinsic line widths and diameters, we refrain from a detailed analysis of virial and tidal stability. However, the detection of GMA-like structures in grand design spirals such as M51 and M100 (Vogel et al. 1988; Rand & Kulkarni 1990; Rand 1995), as well as flocculent spirals like NGC 4414 and NGC 5055 (Sakamoto 1996; Thornley & Mundy 1997; this paper), suggest that GMA-like structures can form in a wide range of galactic environments.

TABLE 2

PROPERTIES OF INDIVIDUAL GMAS

GMA	($\Delta\alpha$, $\Delta\delta$)[a] (arcsec, arcsec)	M_{mol} (10^7 $M_\odot$)	D[b] (pc)
1	(−3.5, 49)	4.6	440
2	(−12, 38)	12	760
3	(−24, 28)	6.9	530
4[c]	(6.1, 15)	27	700
5	(−5.9, 25)	13	480
6[c]	(−3.5, 21)	12	680
7[c]	(−16, 15)	1.2	>270[d]
8[c]	(−12, 1.4)	1.9	480
9	(−7.7, −3.4)	2.0	>380[d]
10[c]	(4.3, −12)	6.1	520
11	(1.9, −21)	4.3	550
12	(4.9, −27)	12	610
13	(16, −19)	18	720

[a] Offset measured from the NIR broadband peak, (α, δ) (J2000) = ($12^h26^m27^s.1$, 31°13′23″.9).

[b] Diameter determined from the average of major and minor axis FWHM. Assumed distance is 18 Mpc.

[c] GMA peaks associated with GMAs defined by Sakamoto 1996: GMA 4 = C1, GMA 6 = C2, GMA 7 = C3, GMA 8 = C4, and GMA 10 = C6.

[d] Clump is unresolved along minor axis.

The surface density distribution of the CO data is shown overlaid with the NIR arm segments in Figure 6. While the arm structures are generally found in the vicinity of enhancements in molecular emission, the variations in brightness of the NIR map are not highly correlated with peaks in the CO map. A number of the H_2 peaks are along arm segments, but two of the four strongest peaks on the northern side of the galaxy lie between segments 3 and 4, and the inner part of segment 5 lies in a region of relatively low molecular surface density. The outermost arm segments to the north and south sides of the galaxy lie in regions where the CO is marginally detected; quantitative assessment of these structures requires more sensitive, large-field observations of CO emission.

The H I surface density map is shown at two different resolutions in Figure 7. The top panel shows the naturally weighted map, in which emission is detected out to $3.3R_{25}$ (6′). This map shows clearly the asymmetry of the large-scale H I distribution, with emission extending to the southeast and, at larger radii, extending westward away from the north end of the major axis. From the naturally weighted map we estimate a total H I mass of 5.0×10^9 $M_\odot$, consistent with that derived by Braine et al. (1993) when scaled to the same distance. The bottom panel of Figure 7 shows the distribution of H I surface density derived from the robustly weighted map, over the same region as in Figure 2. This map show a clear central depression in the H I emission, which is consistent with depressions in CO and Hα emission; we place a limit of 2×10^8 $M_\odot$ on the gas mass within the inner kiloparsec of NGC 4414. The strongest peaks in the robustly weighted map have surface densities (corrected for inclination) of 1.5×10^{21} H atoms cm^{-2} (12 $M_\odot$ pc^{-2}). The average surface density radial profiles of CO and H I, assuming P.A. = 160°, i = 55° (see below), are shown in Figure 8. This comparison confirms that NGC 4414 is a predominantly molecular galaxy: even when scaled to the same beam size, the molecular hydrogen surface density, Σ_{H_2}, exceeds that of H I ($\Sigma_{H\,I}$) by more than a factor of 5 over the region with detected CO emission. At a radius of 30″, the $\Sigma_{H_2}/\Sigma_{H\,I}$ ratio is 15.

The H I emission has a significantly lower resolution than the CO data, but it does suggest alignment of enhanced gas surface density regions along the NIR arm structures (Fig. 7, *bottom panel*). The most striking correlations are along the outermost segments, particularly along the far northern arm (segment 1) which extends to a radius of ∼55″–60″. As Hα emission is not strongly enhanced along segment 1, the alignment of the H I emission suggests that the H I enhancement is not due to the photodissociation of molecular gas by clumps of recent star formation. However, the H I enhancements observed to the south and east of the defined arm segments are consistent both with weak extensions of the designated arms (see Fig. 3), as well as photodissociation by local star formation (see Fig. 1). Higher resolution H I data are needed to determine the detailed morphology of atomic gas in the arm regions.

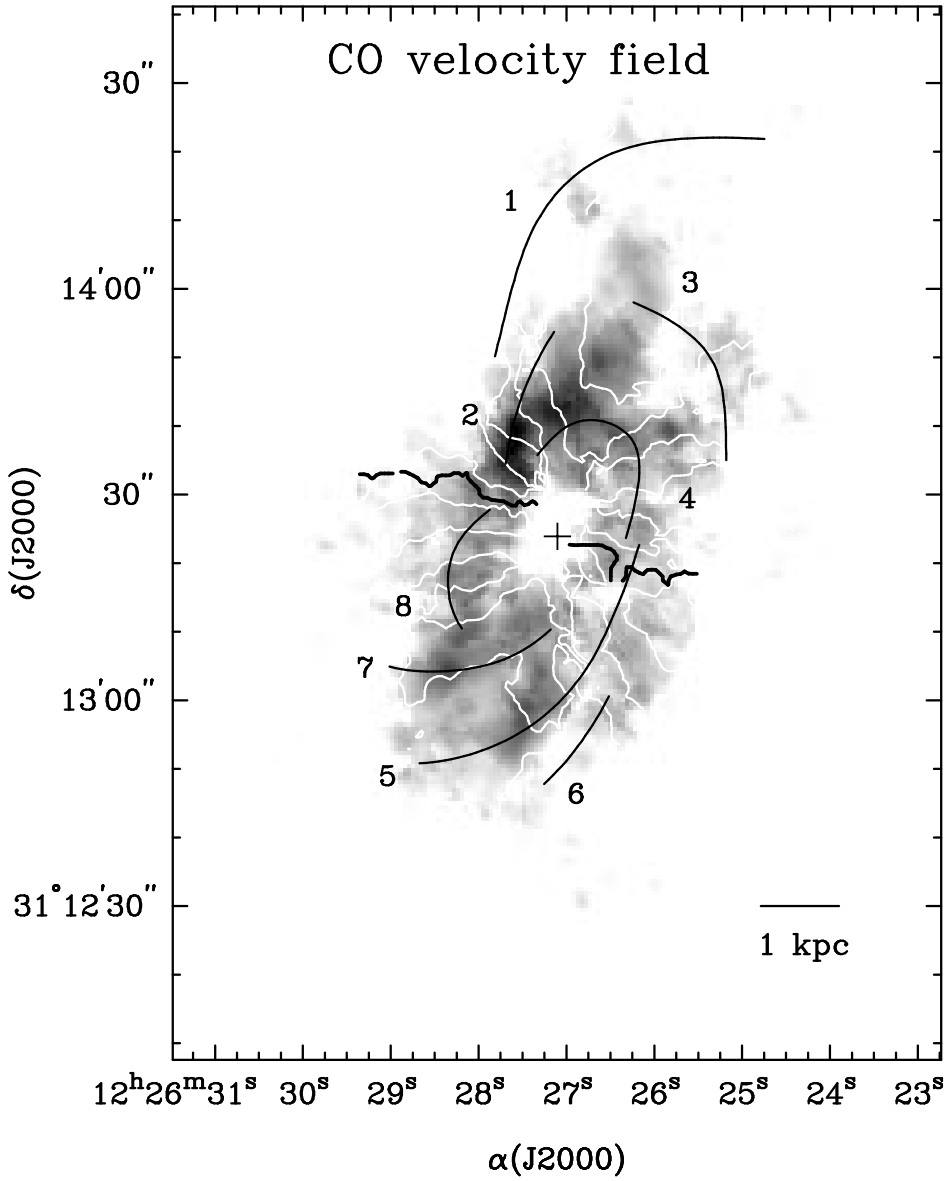

FIG. 9.—CO velocity field of NGC 4414, overlaid on the H_2 surface density map from Fig. 4. Contours are spaced every 32 km s^{-1}, from 518 km s^{-1} to 934 km s^{-1}. Velocity increases from northwest to southeast, with the systemic velocity (V_{LSR} = 726 km s^{-1}) shown as a black contour. The K'-band center is marked with cross, and the NIR arm segments from Fig. 3 are overlaid.

4.2. *Kinematics of Molecular and Atomic Gas*

The CO velocity field derived from the first moment of the CO emission is shown in Figure 9. The velocity field is consistent with that expected for pure circular rotation, with no large-amplitude, ordered deviations from axisymmetry. The CO velocity field (Fig. 9) does not provide high signal-to-noise coverage over several segments, including the longest arm structure on the north side. It does, however, indicate some variations from pure rotation along arm segments 2 and 5, which are also seen in the CO velocity field of Sakamoto (1996).

The H I velocity fields of NGC 4414 (natural and robust weighting) are shown in Figure 10, with isovelocity contours describing a smooth rotational velocity field. The only unusual large-scale kinematic pattern is a slight twist in the outer contours. The velocity field obtained from the first moment of the robustly weighted map (Fig. 10, *bottom panel*) confirms the smoothness of the overall velocity field. Isovelocity contours over the inner disk suggest slight distortions, but velocities are increasingly uncertain in this region due to beam smearing. While the resolution of the H I velocity field is insufficient to isolate velocity features even along the outermost segments, the isovelocity contours along the minor axis are not perpendicular to the major axis in the inner galaxy, suggesting a weak bar or oval distortion. Such a structure could be responsible for weakly driving spiral structure in the inner disk; however, the confirmation of this distortion awaits higher resolution H I observations.

The kinematic parameters of the CO and H I velocity fields were determined by fitting a tilted-ring model implemented as ROTCUR in GIPSY, excluding all points within 20° of the minor axis and using cosine weighting. Profiles showing the variation of rotation velocity (V_{rot}), inclination (i), and position angle (P.A.) with radius are given in Figure 11. The systemic velocity of the CO map is 726 km s^{-1}, and the average P.A. and i over the detected region are 159° and 60°, respectively. The CO rotation curve becomes flat at a

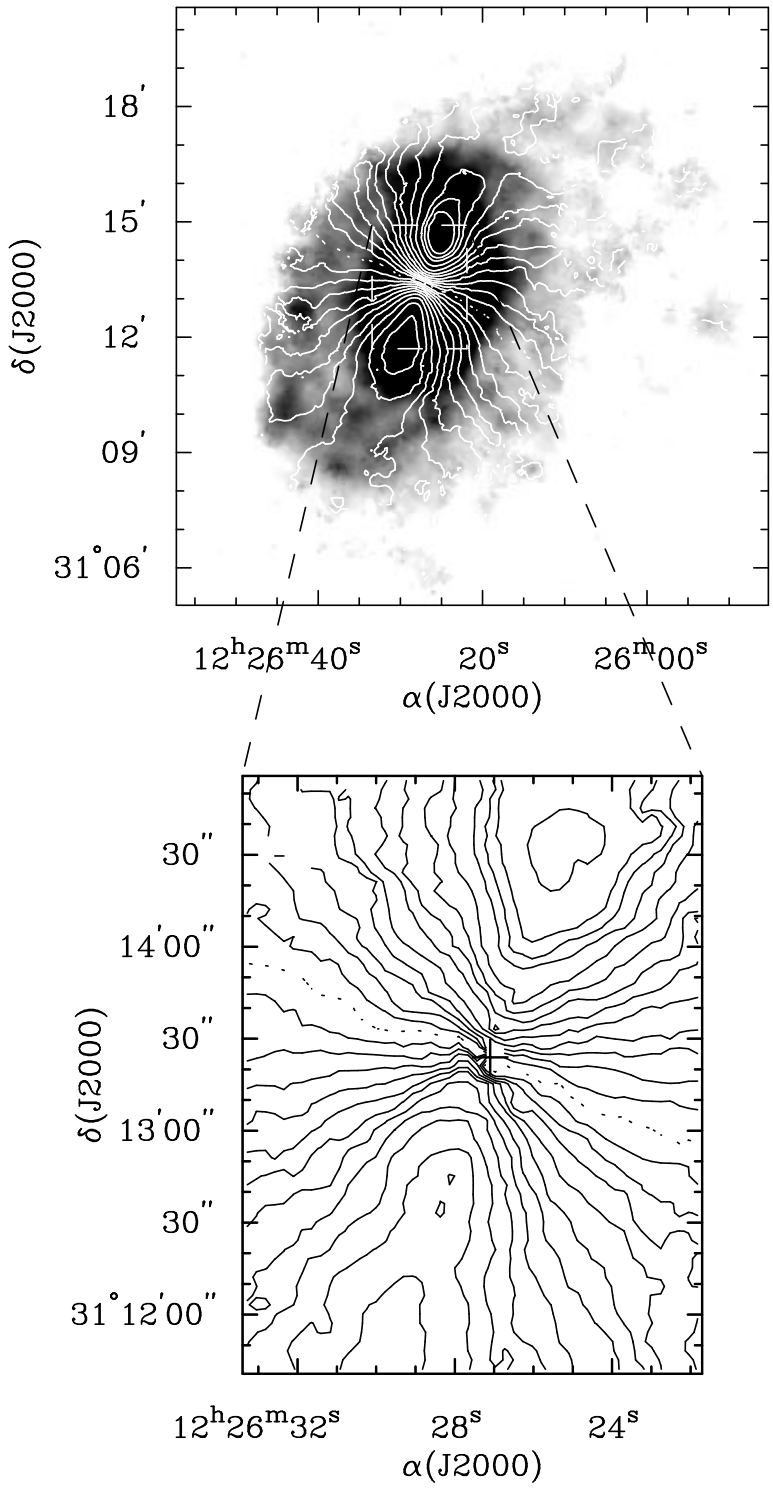

FIG. 10.—H I velocity field, determined from the first moment of the H I map. The top panel shows the velocity field of the naturally weighted map, and the bottom panel shows the velocity field of the robustly weighted map, covering the same region as in Fig. 2. The plus denotes the location of the K' peak. Contours are spaced every 16 km s^{-1}, from 518 km s^{-1} to 934 km s^{-1}. Velocity increases from northwest to southeast. The systemic velocity (V_{LSR} = 726 km s^{-1}) is noted by a dotted contour.

radius of $\sim 30''$, indicating that the innermost CO features are located at radii where the rotation curve is still slowly rising. The average P.A. and i of the H I data over the optical disk ($r < 135''$) are 160° and 55°. While the kinematic P.A. determined from the H I data is consistent with that determined from the CO data, the inclination is 5° smaller. This difference may be caused by greater beam smearing in the H I data. For consistency between data sets, we have used a constant inclination of 55°; note that the average gas surface densities may be overestimated by $\sim 15\%$ by assuming an average inclination of 55°.

The best-fit H I parameters emphasize the asymmetry in the outer disk. While V_{rot}, i, and P.A. are similar on the approaching (north) and receding (south) sides of the galaxy

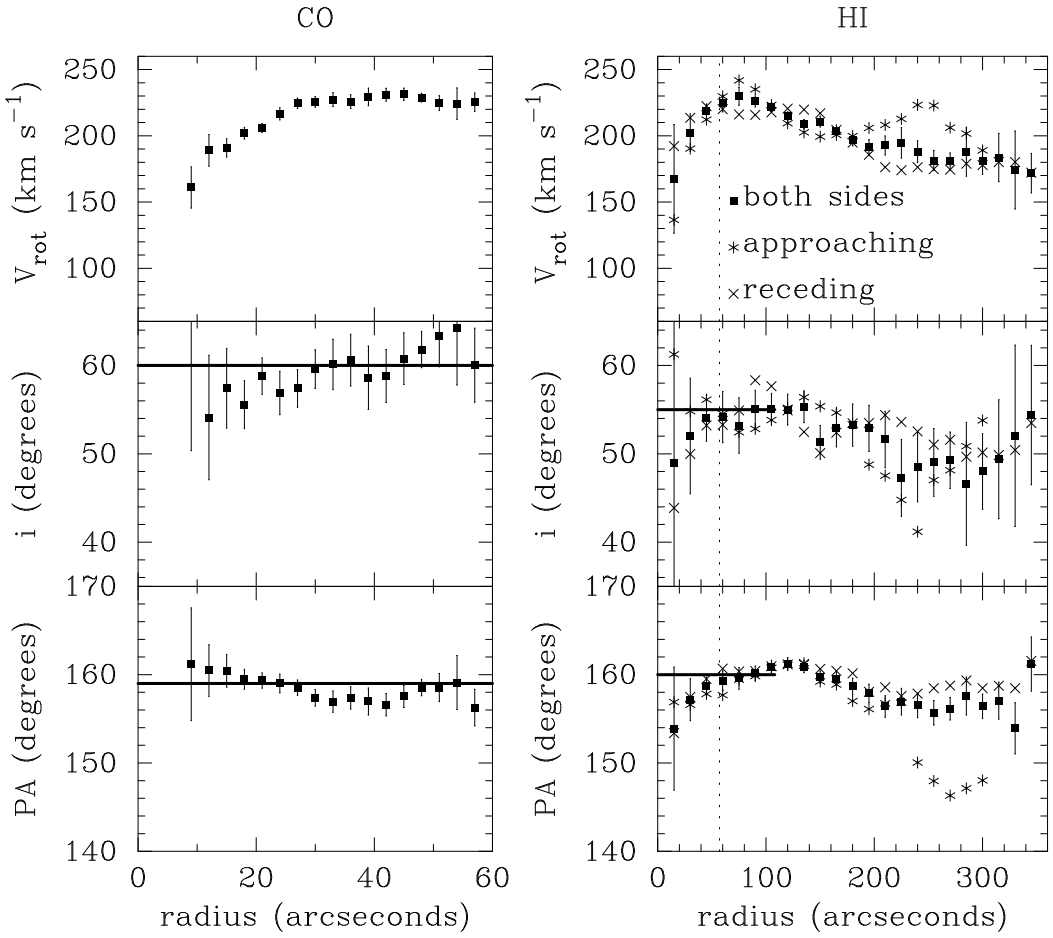

FIG. 11.—*Left panel:* Fit to the full CO velocity field, derived using ROTCUR, showing the variation of rotation velocity (*top*), inclination (*center*), and position angle (*bottom*) with radius. Solid horizontal lines indicate the average values of P.A. (160°) and *i* (55°). *Right panel:* Fit to the velocity field of the robustly weighted H I map, also derived using ROTCUR, showing the same parameters as for the CO velocity field. The fit to the full velocity field is shown in filled squares with error bars. Fits to the approaching side only (*asterisks*) and the receding side only (*crosses*) are also shown. Solid horizontal lines indicate the average values of P.A. and *i* over the optical disk. Dotted vertical lines indicate the radius of the outermost CO data point.

for $r < 200''$, they differ significantly in the outer disk. The inclination has an increasingly poor fit at greater radii, and the position angle of the approaching and receding sides of NGC 4414 differ by as much as 15° in the outer disk. The rotation curve rises to a maximum velocity of 230 km s^{-1} and declines to 175 km s^{-1} in the outer disk. The decrease in velocity at larger radii is more gradual than that reported by Braine et al. (1993). Our rotation velocities determined for radii greater than 240″ (21 kpc) are consistent with a constant rotation velocity of approximately 180 km s^{-1}. There is no evidence that the dark matter halo is unusually small, as suggested by Braine et al. (1993).

4.3. *Mechanisms for Structure Formation*

The varying degree of correlation between CO, H I, and Hα peaks and the NIR arms suggests that any global dynamics in operation are not the dominant factor in structure formation. The structure observed in NGC 4414 is similar to numerical simulations of multiple-arm galaxies, where a marginally unstable stellar disk discourages large-scale, two-arm spiral formation but maintains smaller scale, multiple arm structures in both stellar and gas disks (Elmegreen & Thomasson 1993, see their Fig. 12). While this mechanism is consistent with the evidence for dynamical influences, there are alternative explanations for the observed structure.

Given the high gas surface densities in NGC 4414, it is not clear that the dynamical force organizing the stars and gas must be wave perturbations in the stellar disk, as recently formed gas cloud complexes may provide comparable perturbations in the galactic potential to those of stellar enhancements. The stellar mass radial profile derived by Braine et al. (1997) indicates that the stellar surface density at a radius of ∼30″ is approximately $10^3\ M_\odot\ \mathrm{pc}^{-2}$. NIR arm-interarm contrasts of 1.3 at this radius thus imply enhancements in the stellar surface density of $300\ M_\odot\ \mathrm{pc}^{-2}$, which is within a factor of 2 of the molecular gas surface density enhancements above the median profile derived in § 4.1.

However, the lifetime of a GMA constrains its ultimate ability to influence the formation of structure in the stellar disk. GMAs likely survive only for $\sim 3 \times 10^7$ yr before being destroyed by star formation and shear (Rand 1993; Elmegreen & Thomasson 1993); this lifetime is slightly less than the crossing time for the arm structures observed, which is $0.5–1 \times 10^8$ yr assuming an arm width of 1 kpc (∼10″) and a velocity dispersion of 6–10 km s^{-1}. Thus it is questionable whether the stellar disk would respond quickly enough to form the significant enhancements observed in the NIR. In addition, this mechanism should align the strongest NIR residual emission with peaks in the molecular emission, which is not seen for some prominent

peaks on the north side of the galaxy. The short lives of cloud complexes could explain the off-arm peaks: if these peaks represent recently formed GMAs, there has not yet been enough time for the stellar disk to respond.

Another explanation for the off-arm molecular peaks is that they may be regions where the gas densities are high enough that there is significant extinction, even at NIR wavelengths. Molecular hydrogen surface densities of ~ 300 $M_\odot$ pc^{-2} imply an extinction of $A_V \sim 20$, or $A_K \sim 2$. With high extinction, it is possible that the regions of enhanced NIR emission are actually the lanes between the dust arms (see e.g., Block, Elmegreen, & Wainscoat 1996). However, this requires a high volume filling fraction of molecular gas over large regions in order to significantly affect the morphology in K band. If the NIR arm structures are uniformly covered with gas clouds comparable to Galactic GMCs ($M = 4 \times 10^5\ M_\odot$, $d \sim 20$ pc; Scoville & Sanders 1987), the implied surface density would be approximately $10^3\ M_\odot$ pc^{-2}; comparison with CO observations suggests a maximum filling factor of 25%–30%, which in turn implies $A_K < 1$ when averaged over the width of the arm.

Though this simple analysis suggests it is unlikely that high extinction could create the kiloparsec-scale arm structures observed here, it is possible that patchy extinction could make weakly organized spiral structure appear more flocculent. Perhaps a significant fraction of galaxies classified as "flocculent" appear so due to variations in extinction; this may be particularly true in galaxies with high gas surface densities. Indeed, the extinction toward individual H II regions in M51 measured by van der Hulst et al. (1980) covers the range $A_V = 1$–4; however, the appearance of spiral structure in this case is maintained by large perturbations in the stellar surface density and the organization of all tracers along the spiral arms. An analysis of the importance of extinction in producing flocculent spiral galaxies, a class of objects that is defined primarily by their appearance at optical wavelengths, is currently being pursued by these authors.

It is also possible that there are external influences creating structure in NGC 4414. Observations in all tracers presented in this work show asymmetries on a variety of scales. In the inner disk, CO and Hα images show that the brightest emission extends farther to the north than the south. The large-scale H I extent shows an asymmetry extending to the northwest, to ~ 3 times the optical radius (see Fig. 7). As the velocity of the nearest galaxy on the sky (NGC 4359, located 36′ to the northwest) is significantly different (relative velocity of greater than 500 km s^{-1}), it is unlikely that NGC 4359 and NGC 4414 have had any significant interaction; the extension of H I in the direction of NGC 4359 may simply be a coincidence. Deeper H I observations may be helpful in understanding the origin of the northwest extension of H I.

5. DISCUSSION AND SUMMARY

As a spiral galaxy, NGC 4414 presents an enigma: the gas surface density is high, and there is evidence of dynamical processes producing spiral structures, yet the end result is *not* a well-organized, grand-design spiral. While the presently available kinematic data do not readily provide good limits to the amplitude of streaming motions in NGC 4414, the arm-interarm contrast and extent of observed NIR arm segments is similar to those of NGC 5055, another flocculent galaxy that shows evidence of moderate-amplitude streaming motions (Thornley & Mundy 1997). In NGC 5055, the relatively poor organization of molecular structures along the arms, despite evidence of streaming motions similar in magnitude to those in M100, was suggested to be caused by the lower gas surface density. NGC 4414 suffers no such difficulty: the gas surface densities are comparable to those in M51, a galaxy well known for its strong density waves, yet the spiral structure in NGC 4414 pales in comparison. As M51, M100, and NGC 5055 all have companions, the poorly organized structure in NGC 4414 suggests that tidal interaction with a companion is a critical factor in the formation of well-organized, large-scale structure in spiral galaxies, with more flocculent structures formed by less effective interactions.

The likely presence of both dynamical and stochastic influences in NGC 4414 leaves unclear the formation mechanism for large molecular cloud structures in this galaxy. The detection of GMAs in NGC 4414 suggests that an environment that produces long, well-organized spiral arms is not required to form GMAs; however, the detection of large-mass condensations along the NIR spiral segments casts doubt on their designation as "disk-GMAs," defined to be massive molecular structures formed outside the spiral arm environment (Sakamoto 1996). Some of the strong peaks that lie between arm structures in the northern half of the galaxy may truly be GMAs formed by disk instabilities alone; the determination of their dynamical significance awaits improved kinematic information. The importance of GMAs in the star formation process is also unclear in this case: though NGC 4414 has a somewhat lower global star formation rate than M51, the star formation rates of the two galaxies are comparable within the uncertainties associated with internal extinction. Still, the significance of variations in the star formation process due to dynamical influences is best examined on scales more similar to those of the spiral arms; a later paper will present an arm-interarm comparison of star formation in NGC 4414.

The main points of this paper are summarized as follows:

NIR structure.—The kiloparsec-scale structures detected in NIR broadband images of NGC 4414 have a significant smooth component that is not well matched by the distribution of recent star formation, as traced by Hα emission. The NIR residual structures must therefore represent real enhancements in the old stellar population and, thus, in the gravitational potential. In order to maintain such enhancements in a differentially rotating disk, a large-scale, dynamical influence is needed.

Morphology of gas and stars.—The overall distribution of CO, H I, and Hα emission is generally correlated with the NIR structures and provides supporting evidence that the arm segments have a dynamical origin. However, the poor correlation of some CO and H I peaks with the strongest NIR emission indicates that localized, stochastic effects are also important.

SFR.—The global star formation rate of NGC 4414 is 1.3 $M_\odot$ yr^{-1}. This rate is marginally smaller than the global star formation rate of M51 determined in the same fashion, though extinction introduces large uncertainties in both values.

External influences.—Asymmetries observed in all tracers offer weak evidence of external perturbations, though no obvious companion is present. Deeper observations are needed to determine the significance of the large-scale extension of the H I emission to the northwest.

Partial support for this research was provided by NSF grant AST-9314847 and the State of Maryland through its contributions to the Laboratory for Millimeter-Wave Astronomy. M. D. T. would like to thank PEO International for a Scholar Award, which helped facilitate this work, and the Alexander von Humboldt-Stiftung, for support during the preparation of this work. We would also like to thank J. Braine for providing the single-dish CO data in digital format, S. van Dyk for providing his Hα image prior to publication of an atlas of H II regions by van Dyk & Hodge, and J. Gallimore for helpful guidance in H I data analysis. This work also benefitted from discussions with Christine Wilson, Robert Gruendl, and Natascha Förster-Schreiber.

REFERENCES

Block, D. L., Elmegreen, B. G., & Wainscoat, R. J. 1996, Nature, 381, 674
Braine, J., Brouillet, N., & Baudry, A. 1997, A&A, 318, 19
Braine, J., Combes, F., & van Driel, W. 1993, A&A, 280, 451
Briggs, D. S. 1995a, BAAS, 27, 1444
———. 1995b, Ph.D. thesis, New Mexico Inst. Mining & Tech.
Bruzual, A. G., & Charlot, S. 1993, ApJ, 405, 538
Cepa, J., & Beckman, J. E. 1990, A&A, 239, 85
de Vaucouleurs, G., de Vaucouleurs, A., Corwin, H. G. J., Buta, R. J., Paturel, G., & Fouque, P. 1991, Third Reference Catalogue of Bright Galaxies (New York: Springer)
Deutsch, E. W., & Allen, R. J. 1993, AJ, 106, 1812
Elmegreen, B. G. 1994, ApJ, 433, 39
Elmegreen, B. G., & Elmegreen, D. M. 1986, ApJ, 311, 554
Elmegreen, B. G., & Thomasson, M. 1993, A&A, 272, 37
Elmegreen, D. M., & Elmegreen, B. G. 1982, MNRAS, 201, 1021
———. 1984, ApJS, 54, 127
———. 1987, ApJ, 314, 3
Elmegreen, D. M., Elmegreen, B. G., Lang, C., & Stephens, C. 1994, ApJ, 425, 57
Gerola, H., & Seiden, P. E. 1978, ApJ, 223, 129
Grosbøl, P., & Patsis, P. A. 1996, in New Extragalactic Perspectives in the New South Africa, ed. D. L. Block & J. M. Greenberg (Dordrecht: Kluwer), 251
Gruendl, R. A. 1996, Ph.D. thesis, Univ. Maryland
Kaufman, M., Bash, F. N., Hine, B., Rots, A. H., Elmegreen, D. M., & Hodge, P. W. 1989, ApJ, 345, 674
Kennicutt, R. C., Jr. 1979, ApJ, 228, 394
———. 1983, ApJ, 272, 54
———. 1989, ApJ, 344, 685
Kennicutt, R. C. Jr., & Kent, S. M. 1983, AJ, 88, 1094
Kennicutt, R. C. Jr., Tamblyn, P., & Congdon, C. E. 1994, ApJ, 435, 22
Knapen, J. H. 1993, PASP, 105, 323
Knapen, J. H., Beckman, J. E., Cepa, J., & Nakai, N. 1996, A&A, 308, 27
Lord, S. D., & Young, J. S. 1990, ApJ, 356, 135
McCall, M. L., & Schmidt, F. H. 1986, ApJ, 311, 548
Pierce, M. J. 1994, ApJ, 430, 53
Pogge, R. W. 1989, ApJS, 71, 433
Rand, R. J. 1993, ApJ, 410, 68
———. 1995, AJ, 109, 2444
Rand, R. J., & Kulkarni, S. R. 1990, ApJ, 349, L43
Regan, M. W., & Gruendl, R. A. 1995, Astronomical Data Analysis and Systems IV (San Francisco: ASP), 335
Regan, M. W., & Vogel, S. N. 1994, ApJ, 434, 536 (RV94)
Rix, H. W., & Rieke, M. J. 1993, ApJ, 418, 123
Sakamoto, K. 1996, ApJ, 471, 173
Schild, R. 1977, AJ, 82, 337
Scoville, N. Z., & Sanders, D. B. 1987, in Interstellar Processes, ed. D. J. Hollenbach & H. A. Thronson (Dordrecht: Reidel), 21
Seiden, P. E., & Gerola, H. 1979, ApJ, 233, 56
Seiden, P. E., & Schulman, L. S. 1990, Adv. Phys., 39, 1
Stark, A. A., Elmegreen, B. G., & Chance, D. 1987, ApJ, 322, 64
Strong, A. W., et al. 1988, A&A, 207, 1
Struck-Marcell, C., & Tinsley, B. M. 1978, ApJ, 221, 562
Thornley, M. D. 1996, ApJ, 469, L45
———. 1997, in preparation
Thornley, M. D., & Mundy, L. G. 1997, ApJ, 484, 202
Tilanus, R. P. J., & Allen, R. J. 1993, A&A, 274, 707
Tully, R. B. 1988, Nearby Galaxies Catalog (Cambridge: Cambridge Univ. Press)
van der Hulst, J. M., Kennicutt, R. C., Crane, P. C., & Rots, A. H. 1980, A&A, 195, 38
van Dyk, S. D. 1992, AJ, 103, 1788
Vogel, S. N., Kulkarni, S. R., & Scoville, N. Z. 1988, Nature, 334, 402
Welch, W. J., et al. 1996, PASP, 108, 93
Wilson, C. D. 1995, ApJ, 448, L97